Applied Physics Express

The Japan Society of Applied Physics

Signal enhancement in X-ray Talbot interferometry with a pair of concave and convex parabolic phase gratings

To cite this article before publication: Atsushi Momose *et al* 2024 *Appl. Phys. Express* in press https://doi.org/10.35848/1882-0786/ad9665

Applied Physics Express

Signal enhancement in X-ray Talbot interferometry with a pair of concave and convex parabolic phase gratings

Atsushi Momose[1]*, Pouria Zangi[2], Pascal Meyer[2], Martin Börner[2], Shinji Kobayashi[3], Yichen Fang[3], Ryosuke Ueda[1], Yoshichika Seki[1]

[1]*Institute of Multidisciplinary Research for Advanced Materials, Tohoku University, 2-1-1 Katahira, Aoba-ku, Sendai 980-8577, Japan*

[2]*Institute of Microstructure Technology, Karlsruhe Institute of Technology, Hermann-von-Helmholtz-Platz 1, 76344 Eggenstein-Leopoldshafen, Germany*

[3]*Graduate School of Engineering, Tohoku University, 2-1-1 Katahira, Aoba-ku, Sendai 980-8577, Japan*

X-ray Talbot and Talbot-Lau interferometers consisting of transmission gratings are widely used for X-ray phase imaging, which depicts soft materials. This study exploits the use of a pair of concave and convex parabolic gratings instead of a conventional rectangular phase grating to enhance the phase signal optically. To gain insight into the optimal design, signal enhancement is evaluated by directly measuring the self-image formed downstream of the pair. Increase in the differential phase signals is demonstrated as a function of the distance between the pair, and prospects for deploying this concept into a practical phase imaging technique are discussed.

X-ray transmission images are widely used in non-destructive inspection fields such as medical image diagnosis, security checks, quality inspections, X-ray microscopy, and so on, relying on X-ray absorption contrast. About a century after X-ray discovery, since the 1990s, research on X-ray phase contrast has become active,[1–6] thanks to advances in the manufacturing technology of X-ray optical elements, the spread of high-brightness X-ray sources such as synchrotron radiation, and the development of digital X-ray image detectors. X-ray phase imaging is attracting attention for its ability to visualize light-element materials, which cannot be visualized by conventional X-ray radiography due to insufficient contrast. X-ray Talbot interferometry,[7] including its variations like Talbot-Lau interferometry,[8] is actively studied due to its adaptability with both synchrotron radiation and laboratory-based X-ray sources, using transmission gratings. It is highlighted that three kinds of images mapping absorption, differential phase (or refraction), and scattering (or dark-field signals[9]) caused by a sample are generated simultaneously and can be utilized complementarity. Its practical applications to medicine and non-destructive testing are in progress in collaboration with

*E-mail: atsushi.momose.c2@tohoku.ac.jp

industry.[10–17)]

X-ray phase imaging surpasses conventional radiography because the phase shift cross section is about a thousand times larger than the absorption cross section for light elements. Therefore, the sensitivity of X-ray phase imaging should be a thousand times better in principle. However, such a theoretical sensitivity gain has not been attained practically especially with X-ray Talbot interferometers built in laboratories because of the performance of X-ray tubes, the limited spaces for instrumentation, and so on.

The imaging sensitivity or the signal-to-noise ratio can normally be improved by increasing the X-ray exposure time and/or X-ray flux density, because the uncertainty (or statistical noise) in the refraction signal is inversely proportional to the square root of the total photon number per pixel. In this Letter, apart from such approaches relying on noise reduction, we will discuss a new measure to improve the signal-to-noise ratio by enhancing the signal.

A Talbot interferometer consists of a phase grating (G1) and an amplitude grating (G2), and a sample is normally placed in front of G1.[7,18)] A self-image of G1 is generated by the (fractional) Talbot effect,[19)] and its deformation caused by the sample is analyzed by G2. The sensitivity of X-ray Talbot interferometry is therefore proportional to the distance between G1 and G2 and inversely proportional to their periods. Increasing the G1-G2 distance enhances sensitivity due to a stronger signal. While long interferometers can be easily built at synchrotron radiation facilities, they are not ideal for compact laboratory designs. Current fabrication technology can achieve grating periods of a few microns or larger for high-aspect-ratio structures needed for hard X-rays, while a period below one micron remains a challenging target.[20)]

As the third approach for increasing the sensitivity, we have been studying the signal enhancement by using a pair of concave and convex parabolic gratings in place of the phase grating G1 which normally has a rectangular grating profile.[21)] It was demonstrated that the sensitivity to the minute X-ray refraction caused by a sample could be enhanced without reducing the grating period or elongating the interferometer, utilizing the lens-array effect of the parabolic gratings. However, the pilot demonstration selected grating structures and alignments convenient for the experiment. Consequently, an optimal design guideline for sensitivity-enhanced X-ray phase imaging considering the distance between concave and convex parabolic gratings and the position of the amplitude grating (G2) in relation to the focal lengths of the parabolic gratings has not yet been explored.

Therefore, to gain insight into the optimal design, we conducted experiments to directly measure the self-images downstream of the concave (L1) and convex (L2) parabolic gratings

as a function of the L1-L2 distance. Differential phase images and visibility images were calculated from the self-images by the Fourier-transform method,[22] and the sensitivity enhancement factor was evaluated. In addition, the effect of the lateral shift between L1 and L2 was evaluated.

The parabolic gratings used for the presented experiments were fabricated by the deep X-ray LIGA (Lithographie, Galvanoformung, Abformung) process at the Karlsruhe Research Accelerator (KARA) and at the Institute of Microstructure Technology (IMT), Germany.[20,21] Concave and convex parabolic array structures made of Ni were fabricated on individual Si substrates, and in use the X-ray beam was directed along the substrate surface. Although the imaging field of view in the direction perpendicular to the substrate was therefore limited by the pattern height (several tens of microns), the experiments conducted for this study were performed without any inconvenience. Of course, for various applications in the future, expansion of the field of view should be attained, and strategies for doing so will be discussed later.

The experiments were performed by using monochromatic synchrotron X-rays at BL20XU-med, SPring-8, Japan, where X-rays are available about 200 m downstream from the undulator source. The photon energy of the X-rays was set to 17.0 keV through a double-crystal monochromator. Concave (L1) and convex (L2) parabolic gratings with a period of 10 μm were placed on a single flat plate, as shown in Fig. 1(a). The L1 had a bi-concave shape and L2 had a plano-convex shape, which is similar but not identical to those used in the previous work.[21] The focal lengths of L1 and L2 were designed to be 80 mm and −80 mm for 17.0-keV X-rays, respectively. The actual focal length of L1 (f_1) was experimentally measured to be 92 mm, and it is speculated that the difference from the design occurred because the radius of the curvature of the concaves was slightly larger than the design (429 nm). Although the focal length of L2 (f_2) could not be measured using X-rays, it was possible to infer it from the experimental results, as discussed later. A 30-degree wedge of a set square made of polymethyl methacrylate (PMMA) was placed in front of L1 on the same table (note that the tip of the wedge was not sharp). The intensity of X-rays downstream of the L1-L2 pair was recorded by a high-resolution X-ray image detector consisting of a LuAG(Ce) scintillator 10 μm in thickness, a lens system (AA50, Hamamatsu, Japan), and a sCMOS camera (ORCA-Flash4.0, Hamamatsu, Japan), whose effective pixel size was 0.49 μm. The L1-L2 distance (Z) was set to 20, 30, 54, 60, 70, and 92 mm, and the L2-detector distance (L) was set to $17 + 50n$ [mm], where $n = 1, 2, \ldots, 9$, for each setting of Z. The lateral position between L1 and L2 was changed by rotating the plate slightly by $\Delta\Theta$ about the vertical axis, and the change in the

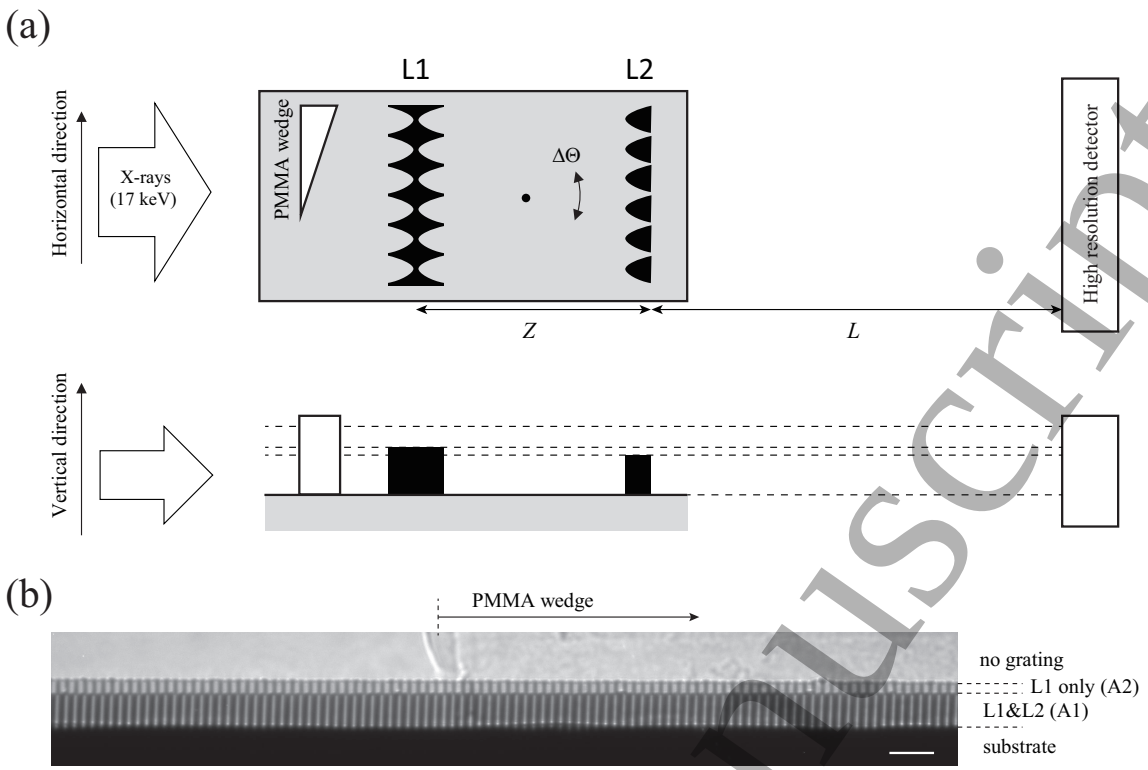

Fig. 1. Top view and side view of the experimental setup (a) with parabolic gratings (L1 and L2) placed on a common plate and a representative self-image (b) observed directly by a high-resolution detector. A 30-degree wedge made of polymethyl methacrylate (PMMA) was placed in front of L1. Due to a slight difference in the pattern heights of L1 and L2, self-images in area A1 (through the L1-L2 pair), area A2 (through only L1), and the area without gratings were simultaneously recorded by a high-resolution image detector, as shown in (b). The lateral position between L1 and L2 was changed by rotating the plate by a small angle ΔΘ, and a movie of the self-image is given in Movie 1 in Supplement. Scale bar: 50 μm.

self-image pattern was also studied.

Figure 1(b) shows a representative self-image observed when Z = 54 mm and L = 117 mm. Since the pattern height of L1 was slightly larger than that of L2, the self-image pattern observed downstream consisted of areas through the L1-L2 pair (A1), L1 only (A2), and without gratings. Note that only the propagation-based phase contrast (edge enhancement)[23] of the wedge sample is seen in the area without gratings. A series of self-images observed varying ΔΘ are presented in Movie 1 in Supplement.

Differential phase images calculated from Movie 1 using the Fourier transform method[22] are provided in Movie 2 in Supplement. Figure 2(a) highlights one of the frames, showing only areas A1 and A2. Movie 2 indicates that the differential phase signal remained invariant within ± 0.02 rad on the scale of the self-image fringe phase as ΔΘ was varied; that is, the measurement was not affected by the lateral position change between L1 and L2. This implies

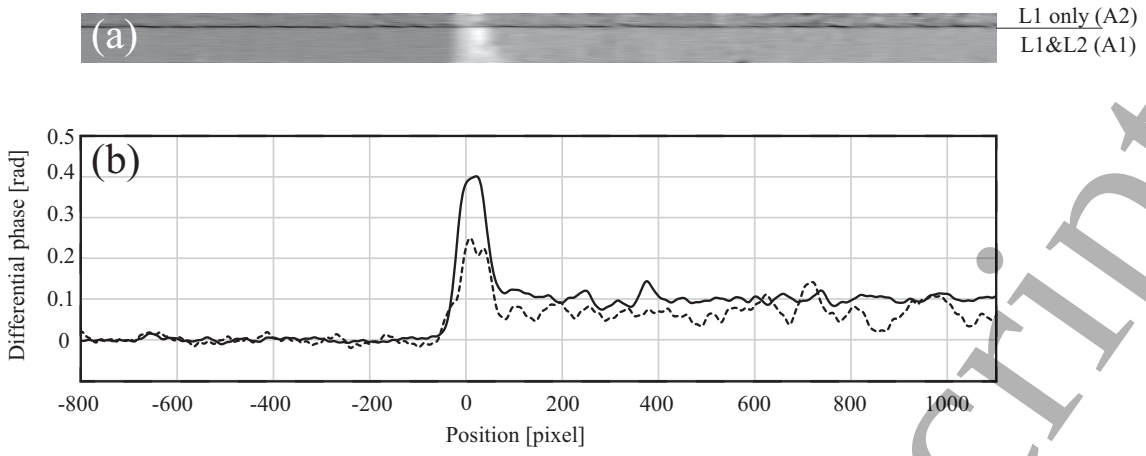

Fig. 2. Differential phase image (a) obtained from the self-image presented in Fig. 1. Profiles at A1 and A2 are represented by the solid and dashed lines, respectively (b).

that this optical configuration is robust against mechanical perturbation, grating imperfection, and misalignment, ensuring that the measurements of the differential phase in this work are free from such concerns.

Figure 2(b) shows the profiles of the differential phase in Fig. 2(a), where the solid line and dashed line are those at A1 and A2, respectively. The differential phase signal in A1, within the slope region of the wedge, was actually higher compared to that in A2. The strong signal seen at the tip of the wedge sample is likely due to the tip being chipped, and signal enhancement is seen here as well.

In the previous study,[21] it was assumed that a concave lens unit and a convex lens unit are aligned on a common principal axis. Therefore, the aforementioned fact that the differential phase signal was almost invariant against $\Delta\Theta$ is of practical significance beyond

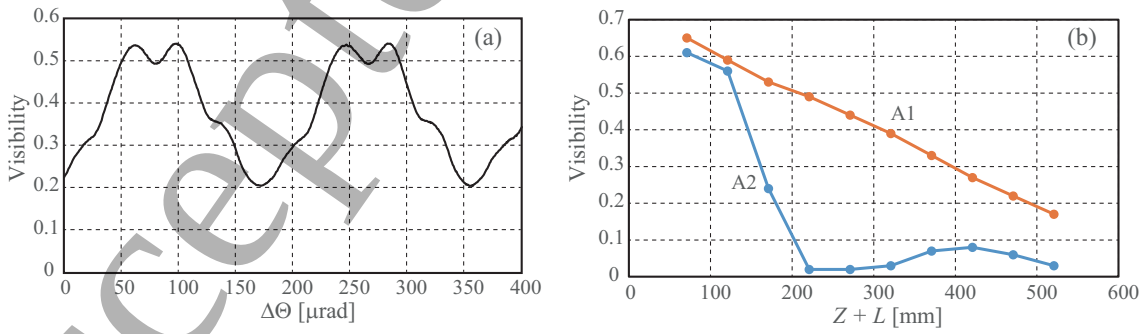

Fig. 3. (a) The visibility of self-images as a function of $\Delta\Theta$ when Z = 54 mm and L = 117 mm. The visibility variation has a period of 178 μrad, which corresponds to a lateral shift of one period between L1 and L2. (b) Variation of the maximum self-image visibility along the optical axis.

the assumption. However, we need to pay attention to the fact that the visibility depended on ΔΘ, which is shown in Fig. 3(a) and Movie 3 in Supplement. The visibility varied in a range between 0.2 and 0.54 with a period of 178 μrad, which corresponds to a lateral shift of one period between L1 and L2. Although it is possible to obtain the differential phase signal throughout the period, it is suggested that the displacement between L1 and L2 exceeding the half of the period causes the increase of noise because of visibility reduction. Figure 3(b) shows the variation along the optical axis of the maximum visibility through ΔΘ scans. While the visibility at A2 decreased rapidly, the visibility at A1 kept higher values. This implies that the self-image downstream of the L1-L2 pair showed a needle-beamlet feature, which was also suggested in the previous work.[21)]

Next, assuming that the slope region of the wedge sample causes constant refraction (i.e., constant differential phase signal), the signals were area-averaged in A1 and A2 to remove the signal fluctuation caused by the surface roughness of the wedge and photon statistics. The result is summarized in Fig. 4, where measured differential phase signals are plotted as a function of the distance from L1 ($Z + L$) for the settings of different L1-L2 distances (Z). The

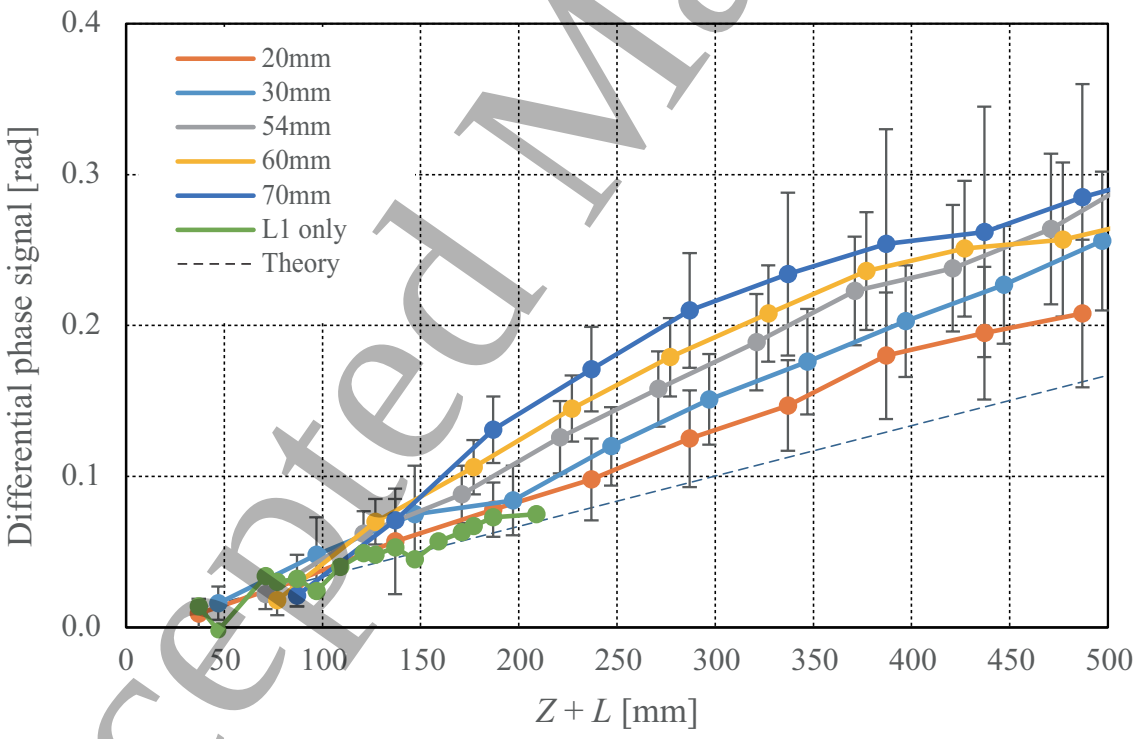

Fig. 4. Differential phase signals of the wedge sample measured as a function of the distance from L1 ($Z + L$). The dashed line shows the theoretical value when a rectangular phase grating is placed at the position of L1. The result at A2 (L1 only) almost coincides with the dashed line. Other results show the signals detected at A1. The numbers shown in the legend are the L1-L2 distances (Z).

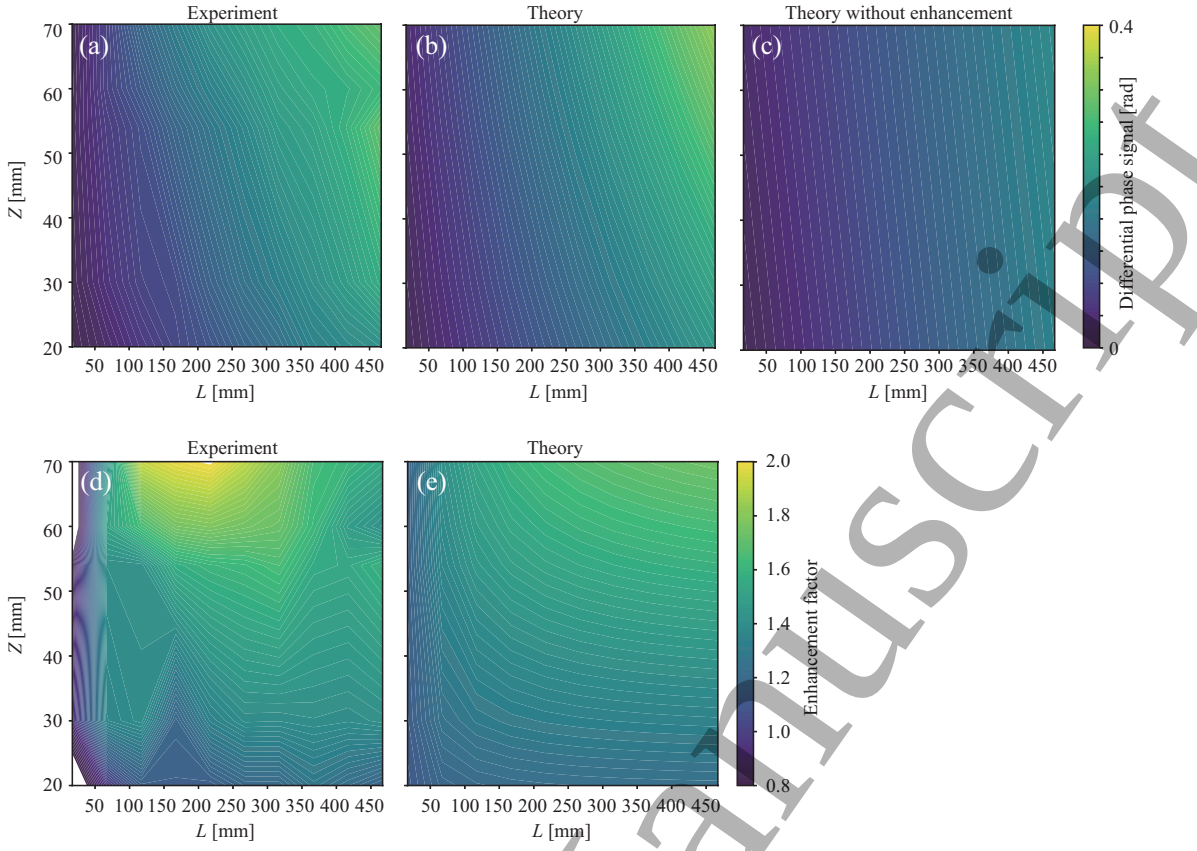

Fig. 5. Differential phase signal obtained by the experiment (a) and theory (b) as functions of Z and L. The theoretical differential phase signal without enhancement is given in (c). The signal enhancement factors (M) obtained from the experimental results and the theory are given in (d) and (e), respectively.

plots at A2 (L1 only) are shown together. The error bars correspond to the standard deviations of the averaged signals. It is speculated that the error bars increased with distance from L1 due to the decrease in the visibility of the self-image, as shown in Fig. 3(b).

The data at A2 (L1 only) corresponds to the conventional signal directly relating to the refraction by the sample and is consistent with the theory (dashed line) predicted if only a rectangular phase grating were placed at the position of L1. The others are plots of the data when Z = 20, 30, 54, 60, and 70 mm. At any L1-L2 distance, the differential phase signals were actually enhanced, and the slopes of the plots were steeper for larger Z, which indicates that the enhancement factor increased with Z.

Here, we consider the signal enhancement factor M given by

$$M = 1 - \frac{1}{f_2}\frac{LZ}{L+Z}, \tag{1}$$

following the definition in the previous work.[21] Contour maps of the differential phase signal as functions of Z and L are given in Figs. 5(a), 5(b), and 5(c), which are those obtained

by the experiment, the theoretical calculation using eq. (1), and the theoretical calculation without enhancement, respectively. Note that, in calculating the theoretical values, f_2 should be known. Because we only had a design value (−80 mm), a fitting analysis was conducted between the theoretical and experimental results. We found that $f_2 = -82.8$ mm provided the best fit. The theoretical differential phase signal was calculated using this value, resulting in Fig. 5(b). Compared to the differential phase signal without enhancement shown in Fig. 5(c), the experimental results clearly demonstrate the signal enhancement effect. Figures 5(d) and 5(e) show the comparison of M between the theory and the experiment. The tendency that M is larger for greater Z and L is confirmed, although some systematic deviation remains in the experimental results. These deviations are thought to be due to the significant error bars shown in Fig. 4 and the shape deviations of the gratings from the design.

It is thus confirmed by experiments that the enhancement factor can be described by eq. 1. The question in this study was rather whether there are any optimal relation in distances between gratings. Regarding the distance between L1 and L2 (Z), a larger Z is preferable. However, when Z reaches 92 mm, which is comparable to f_1, the focal position of L1 coincides with L2, leading to instability in the differential phase signal (see Fig. S1 in Supplement). Therefore, the value for Z is recommended to be greater than $f_1/2$ and safely less than f_1.

While the position of G2 is important in optical design of an X-ray Talbot interferometer, the presented results of varying L suggest that there is no strong positional recommendation for G2. This is because the L1-L2 pair formed needle beamlets within the range of this experiment, as shown in Fig. 3(b). Note that the G1-G2 distance is calculated to be 685 mm under the conditions of this study when a $\pi/2$ phase grating is employed for G1 and the Talbot order is 1/2. Therefore, the optical design with the L1-L2 pair can be more flexible and more compact than that of a conventional Talbot interferometer.

In X-ray Talbot interferometry, the scattering image (or dark-field signals) can be obtained from the reduction in visibility. How about the signal enhancement in the scattering images? In the previous work,[21] an example obtained for a leaf sample was presented in its supplement, and a signal enhancement was actually seen. It is speculated that the enhancement factor M is common with that for the scattering image since the small-angle scattering field from a sample is considered to be amplified in the same manner as that for refraction. However, the presented experiment was performed for a PMMA sample, with which visibility reduction was not expected, and no theoretical formulation of this problem has currently been established. Therefore, as a next step, the visibility reduction of the self-images downstream of the L1-L2 pair should be studied with a known scattering sample.

Next, we consider a practically important question: can the presented signal enhancement concept be applied to Talbot-Lau interferometry? Talbot interferometry requires a microfocus X-ray tube, whereas Talbot-Lau interferometry allows the use of a standard focus X-ray generator, allowing for faster measurements. A Talbot-Lau interferometer is constructed by adding an amplitude grating (so-called G0) on the source side to a Talbot interferometer. The function of G0 is to form a virtual array of microfocus X-ray sources, and each source forms a self-image of G1 on G2 and is overlaid with the self-image formed by the neighbor source constructively. When G0 is placed upstream of the L1-L2 pair, the change in the direction of the X-ray beams from the virtual sources to the pair corresponds to the $\Delta\Theta$ scan in the presented experiments. The aforementioned result that the differential phase signal was constant through the $\Delta\Theta$ scan is meaningful in considering the application to the Talbot-Lau configuration. As a result, we expect that a Talbot-Lau X-ray interferometer will be feasible with the presented signal enhancement concept although it should be confirmed experimentally.

Note that the selection of the period of G0 and the position of G2 must satisfy a geometrical constraint so that the self-image keeps sufficient visibility. Conventionally, the G1-G2 distance is selected from discrete positions indexed by the Talbot order,[7,8] and then the period of G0 is determined. However, thanks to the needle-beamlet feature of the self-image in the presented configuration, the position of G2 can be selected freely, and then the period of G0 is determined by the G2 position geometrically. Thus, the optical design for the Talbot-Lau configuration is also flexible under the signal enhancement concept.

For conventional Talbot and Talbot-Lau interferometry, the sample can be placed either in front of G1 or between G1 and G2. However, for the presented signal enhancement configuration, the sample cannot be placed between the L1-L2 pair and G2 (i.e., downstream of the pair) because the signal enhancement occurs at the pair.

The presented experiment was performed with monochromatic X-rays from synchrotron radiation. When the signal enhancement concept is introduced in laboratories, we need to pay attention in using a polychromatic cone beam. It is well known that X-ray Talbot (and Talbot-Lau) interferometers work sufficiently with polychromatic X-rays. However, it is not clear how the signal enhancement is affected by the X-ray spectrum. The effect of X-ray beam quality on the enhancement factor is also a concern to be studied in the near future.

To deploy the sensitivity enhancement concept into a practical phase imaging technique, it is also important to broaden the field of view. As mentioned, the current gratings have parabolic surfaces perpendicular to the substrate, and therefore the pattern height (several tens of microns) limits the field of view. To circumvent this limitation, the parabolic surfaces

should be made in a plane parallel to the grating substrate so that an X-ray beam can be introduced perpendicular to the substrate. Then, such a parabolic grating can be used in the same way as the conventional setups of X-ray Talbot(-Lau) interferometers, and the field of view can be expanded to the area where the grating pattern is formed.

Regarding the structures for such 2.5-dimensional gratings, there are two targets in developments: one is a linear grating having parabolic grooves in depth or bumps in height, and the other is a two-dimensional grating having an array of units of the paraboloid of revolution. The former can sense refraction and scattering only in the direction perpendicular to the grooves (bumps), the situation of which is the same as that with conventional Talbot(-Lau) interferometers with linear gratings. If the latter is realized, corresponding to a two-dimensional grating, it would enable the simultaneous sensing of refraction and scattering in two directions.

However, fabricating such 2.5-dimensional grating structures by conventional lithographic approaches is not straightforward. Two-photon lithography[24] is expected as an attractive technique for this purpose.

Acknowledgment

This work was financially supported by ERATO (Grant No. JPMJER1403) and SICORP (Grant No. JPMJSC1809), Japan Science and Technology Agency, JSPS KAKENHI Grant No. JP24K01370 and the BMBF via DLR under Contract No. 01DR18015A, Germany. The authors acknowledge the support of the Karlsruhe Nano Micro Facility (KNMFi), a Helmholtz Research Infrastructure at Karlsruhe Institute of Technology. The experiment was performed under the approval of the SPring-8 committee (2022B1356).

References

1) R. Fitzgerald, *Phys. Today* **53**(7), 23 (2000).
2) A. Momose, *Jpn. J. Appl. Phys.* **44**, 6355 (2005).
3) K. Nugent, *Adv. Phys.* **59**, 1 (2010).
4) A. Bravin, P. Coan, and P. Suortti, *Phys. Med. Biol.* **58**, R1 (2013).
5) A. Momose, *Phys. Medica* **79**, 93 (2020).
6) L. Birnbacher, E.-M. Braig, D. Pfeiffer, F. Pfeiffer, and J. Herzen, *Eur. J. Nucl. Med. Mol. Imaging* **48**, 4171 (2021).
7) A. Momose, S. Kawamoto, I. Koyama, Y. Hamaishi, K. Takai, and Y. Suzuki, *Jpn. J. Appl. Phys.* **42**, L866 (2003).
8) F. Pfeiffer, T. Weitkamp, O. Bunk, and C. David, *Nat. Phys.* **2**, 258 (2006).
9) F. Pfeiffer, M. Bech, O. Bunk, P. Kraft, E. F. Eikenberry, Ch. Brönnimann, C. Grünzweig, and C. David, *Nat. Mat.* **7**, 134 (2008).
10) A. Tapfer, M. Bech, A. Velroyen, and F. Pfeiffer, *Proc. Natl. Acad. Sci. USA* **109**, 15691 (2012).
11) J. Tanaka, M. Nagashima, K. Kido, Y. Hoshino, J. Kiyohara, C. Makifuchi, S. Nishino, S. Nagatsuka, and A. Momose, *Z. Med. Phys.* **23**, 222 (2013).
12) T. Koehler, H. Daerr, G. Martens, N. Kuhn, S. Löscher, U. van Stevendaal, and E. Roessl, *Med. Phys.* **42**, 1959 (2015).
13) S. Bachche, M. Nonoguchi, K. Kato, M. Kageyama, T. Koike, M. Kuribayashi, and A. Momose, *Sci. Rep.* **7**, 6711 (2017).
14) K. Willer, A. A. Fingerle, L. B. Gromann, F. De Marco, J. Herzen, K. Achterhold, B. Gleich, D. Muenzel, K. Scherer, M. Renz, B. Renger, F. Kopp, F. Kriner, F. Fischer, C. Braun, S. Auweter, K. Hellbach, M. F. Reiser, T. Schroeter, J. Mohr, A. Yaroshenko, H. I. Maack, T. Pralow, H. van der Heijden, R. Proksa, T. Koehler, N. Wieberneit, K. Rindt, E. J. Rummeny, F. Pfeiffer, and P. B. Noël, *PLoS One* **13**, e0204565 (2018).
15) M. Kageyama, K. Okajima, M. Maesawa, M. Nonoguchi, T. Koike, M. Noguchi, A. Yamada, E. Morita, S. Kawase, M. Kuribayashi, Y. Hara, S. Bachche, and A. Momose, *NDT E Int.* **105**, 19 (2019).
16) M. Viermetz, N. Gustschin, C. Schmid, J. Haeusele, M. von Teuffenbach, P. Meyer, F. Bergner, T. Lasser, R. Proksa, T. Koehler, and F. Pfeiffer, *Proc. Natl. Acad. Sci. USA* **119**, e2118799119 (2022).
17) S. van Gogh, M. Rawlik, A. Pereira, S. Spindler, S. Mukherjee, M. C. Zdora, M. Stauber,

R. Alaifari, Z. Varga, and M. Stampanoni, *Opt. Express* **31**, 9052 (2023).

18) T. Weitkamp, A. Diaz, C. David, F. Pfeiffer, M. Stampanoni, P. Cloetens, and E. Ziegler, *Opt. Express* **13**, 6296 (2005).

19) J. P. Guigay, *Opt. Acta* **18**, 677 (1971).

20) P. Meyer and J. Schulz, Chapter 16 - Deep x-ray lithography. In Qin, Y. (ed.) Micromanufacturing Engineering and Technology (Second edition), Micro and Nano Technologies, pp. 365-391, (William Andrew Publishing, Boston, 2015).

21) P. Zangi, K. Ikematsu, P. Meyer, H. Takano, Y. Wu, J. Gutekunst, M. Börner, A. Last, J. G. Korvink, and A. Momose, *Sci. Rep.* **13**, 9624 (2023).

22) M. Takeda, H. Ina, and S. Kobayashi, *J. Opt. Soc. Am.* **72**, 156 (1982).

23) A. Snigirev, I. Snigireva, V. Kohn, S. Kuznetsov, and I. Schelokov, *Rev. Sci. Instrum.* **66**, 5486 (1995).

24) J. Fischer and M. Wegener, *Laser Photonics Rev.* **7**, 22 (2013).